materials

MDPI

Article

The Coupling Effect of O_2 and H_2S on the Corrosion of G20 Steel in a Simulating Environment of Flue Gas Injection in the Xinjiang Oil Field

Xiankang Zhong [1], Yanran Wang [1], Jianjun Liang [2], Long Chen [2] and Xiaoqin Song [1,*]

[1] School of Oil and Natural Gas Engnieering, Southwest Petroleum University, Chengdu 610500, China; zhongxk@swpu.edu.cn (X.Z.); wyr201621000527@163.com (Y.W.)
[2] Engineering Technology Institute, Xinjiang Oil Filed Company, CNPC, Karamay 834000, China; liangjj@petrochina.com.cn (J.L.); cyycl@petrochina.com.cn (L.C.)
* Correspondence: songxiaoqin@126.com; Tel.: +86-028-83037070

Received: 16 August 2018; Accepted: 3 September 2018; Published: 6 September 2018

Abstract: Flue gas injection for heavy oil recovery has received a great deal of attention, because it is more cost effective than lots of other injection methods. However, the corrosion could occur easily, because the flue gas usually contains corrosive gases such as CO_2, H_2S, and O_2. In this work, the corrosion behaviors of G20 steel in flue gas injection environment simulating Xinjiang oil field (China) were investigated using weight loss measurement and surface characterization techniques. The effect of environments including the O_2-containing environment, the H_2S-containing environment, and the O_2-H_2S-coexisting environment on the corrosion of G20 steel in gas phase and liquid phase was discussed. The results show that the corrosion rate of G20 steel in the O_2-H_2S-coexisting environment is much higher than the sum of corrosion rates of the O_2-containing environment and the H_2S-containing environment, regardless of the gas phase and the liquid phase. This indicates that there is a coupling effect between O_2 and H_2S, which can further accelerate the corrosion of steel in O_2-H_2S-coexisting environment. The results of surface characterization demonstrate that in a typical flue gas injection environment, the corrosion products are composed of $FeCO_3$, FeS, FeO(OH), and elemental sulfur. Elemental sulfur could obviously accelerate the corrosion of steel. Therefore, it can be considered that the coupling effect of O_2 and H_2S on corrosion of G20 steel in flue gas injection environment is caused by the formation of elemental sulfur in corrosion products.

Keywords: O_2 Corrosion; H_2S Corrosion; Combined Effect; Flue Gas Injection

1. Introduction

Flue gas injection for heavy oil recovery has received a great deal of attention, because it is more cost effective than lots of other injection methods such as natural gas injection [1]. The flue gas as an injectant for enhanced oil recovery is usually composed of multiple components including N_2, CO_2, O_2, H_2S, hydrocarbons, and water vapor. It is well known that the presence of CO_2, O_2, and H_2S in a wet environment may cause corrosion of metal and alloys. Therefore, there is high corrosion risk for the surface piping and subsurface tubulars in flue gas injection process. Usually, two main strategies are employed to minimize the potential of corrosion: (I) reduce the oxygen content to a minimum by conducting the combustion in a fuel-rich environment and (II) eliminate the possibility of vapour condensation by ensuring that the flue gas is always above its dew point [2]. However, the corrosion cannot still be completely avoided, especially during the practical production process that faces the complex environment.

According to the composition of flue gas mentioned above, in the presence of aqueous solution or water vapor, CO_2, O_2, and H_2S would cause corrosion of metal materials including surface injection piping and subsurface tubulars. CO_2 corrosion has been extensively investigated in the past decades [3–8]. Great progress has been made on CO_2 mechanisms and CO_2 corrosion prediction based on the dedicated efforts of researchers. However, the presence of O_2 and H_2S in CO_2-containing environment makes the corrosion progress more complicated.

In CO_2-O_2 corrosive environment, as a strong oxidant, O_2 could not only directly participate the cathodic reduction reaction during the corrosion process but also change the formation of corrosion products. For example, Choi et al. investigated the O_2 effect on the corrosion of carbon steel in supercritical CO_2-water environments. It was found that the corrosion rate of carbon steel increased with the addition of O_2 to the system due to the inhibition effect of O_2 on the formation of protective $FeCO_3$ [9]. Sun et al. also found that O_2 could inhibit the formation of $FeCO_3$ and dominate the corrosion process in the supercritical CO_2-H_2O-O_2 system [10]. Lin et al. reported that in the CO_2-O_2 environment, dissolved O_2 damaged the integrity of corrosion scale of 3Cr steel by precipitation of $Fe(OH)_3$ at localized area, which caused the non-uniform distribution of Cr, leading to the pitting corrosion and high corrosion rate [11].

The presence of H_2S in the CO_2-containing environment can significantly change the corrosion progress and mechanism of metal and alloys. Abelev et al. studied the effect of H_2S on Fe corrosion in CO_2-saturated brine and found that small H_2S concentrations (5 ppmv) showed an inhibition effect on corrosion and higher H_2S (>50 ppmv); the corrosion rate increased rapidly, but it was still below the corrosion rate for the H_2S-free solution [12]. Choi et al. found that the addition of low-level (100 ppmv) H_2S into CO_2 saturated 1 wt % NaCl at pH 3 and 4 induced a rapid decrease in the corrosion rate of 1018 carbon steel. This inhibition effect was attributed to the formation of thin FeS film on the steel surface that suppressed the anodic dissolution [13]. Sun et al. pointed out that a low concentration (2000 ppmv) of H_2S accelerated the corrosion rate of X65 steel owing to the additional cathodic reaction and the water phase precipitation promoted by H_2S in supercritical CO_2-H_2O-H_2S system [10].

As mentioned above, the effect of a single component (either O_2 or H_2S) on the corrosion in the CO_2-containing environment has been widely investigated. However, studies related to the corrosion in CO_2-containing environment where O_2 and H_2S exist simultaneously are still limited [10,14–16]. To our best knowledge, the coupling effect of O_2 and H_2S in the simulated flue gas injection environment has been rarely reported.

Flue gas injection as an enhanced oil recovery technique has been put on the agenda in Xinjiang oil field (China), where the flue gas contains 15 mol % CO_2, 1.5 mol % O_2, 1.2 mol % CH_4, 600 ppmv H_2S, and about 82 mol % N_2. The composition of flue gas indicates that it is highly corrosive for surface piping and subsurface tubulars if this gas is accompanied by the water vapour condensation. Therefore, the investigation on corrosion of metal materials in the simulating flue gas injection environment is highly significant for the assessment of safety risk prior to the implementation of this project. In this work, the coupling effect of O_2 and H_2S on the corrosion of surface piping (G20 steel) in the simulating flue gas injection environment in the Xinjiang oil field was investigated using weight loss measurement and surface characterization techniques.

2. Materials and Methods

2.1. Materials and Solution

The specimens used in this work were cut from a G20 steel pipe with the following chemical composition (wt %): C 0.18, Si 0.21, Mn 0.5, P 0.03, and S 0.03, with Fe making up the balance. The starting microstructure of G20 steel characterized using electron backscatter diffraction (EBSD, a Zeiss-Crossbeam XB 1540 FIB scanning electron microscope with a Hikari camara, EDAX, AMETEK, Inc. America) is shown in Figure 1. It is demonstrated that G20 steel mainly contains ferrite and cementite (Fe_3C), and the grain size distribution is homogenous. The cementite mainly distributes at

the grain boundary. The presence of ferrite and cementite can also be confirmed in the X-ray diffraction (XRD) results in Section 3.

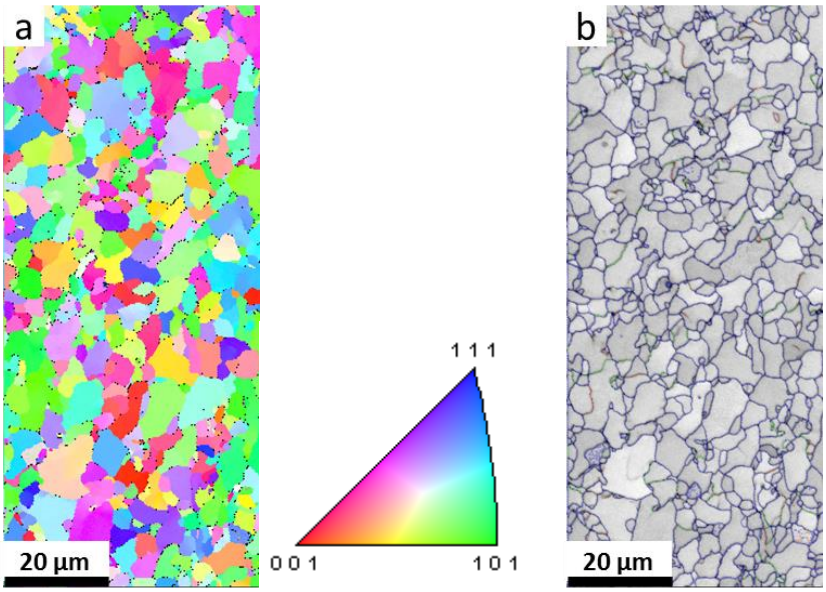

Figure 1. EBSD measurements of G20 steel: (**a**) inverse pole figure map; (**b**) grain boundary map.

The specimens used for the weight loss measurements and surface analysis were cuboids with dimension of 50 mm × 10 mm × 3 mm. Prior to the experiment, each specimen was grounded sequentially using up to 800 grit SiC paper, degreased in an ultrasonic bath with acetone for 10 min, rinsed in ethanol, and dried under the nitrogen flow. The weight of the specimen was taken using an analytical balance with the accuracy of 0.1 mg. Each experiment was performed by exposing five specimens to the simulated flue gas injection environment in autoclave. Three specimens were used for weight loss measurements; the fourth and the fifth were used for surface analysis.

Corrosive solution, which was made up from analytical grade reagents and deionized water, simulated the formation water in Xinjiang oil field; its ionic compositions are listed in Table 1. The total salinity was 9254 mg/L. The solution pH was 7.0. Prior to the experiment, the corrosive solution was deaerated by purging CO_2 (99.99%) gas for 4 h.

Table 1. The ionic compositions of corrosive solution.

Ions	Concentration (mg/L)
Ca^{2+}	125
Mg^{2+}	35
Cl^-	3940
HCO_3^-	1894
SO_4^{2-}	134
$Na^+ + K^+$	3126

2.2. Corrosion Experiment in Autoclave

A 6 L Hastealloy C276 autoclave was used for the corrosion experiment in the present work. The schematic is shown in Figure 2. Two corrosive environments including gas phase and liquid phase were made simultaneously in the one autoclave. Gas phase environment is closer to environment of flue gas injection. As a comparison, the corrosion of G20 steel in liquid phase was also studied. Five specimens for weight loss measurements and surface analysis were mounted into the Teflon holder in the gas phase. Also, other five specimens were installed on the holder in the liquid phase, as is shown in Figure 2. Then, the autoclave was closed and vacuumed by a vacuum-pumping

system. 2.5 L of deaerated solution was then introduced into the autoclave. After the autoclave was heated to 60 °C, CO_2, O_2, and H_2S were injected into the autoclave to a desired partial pressure or concentration. Finally, a booster pump was used to add N_2 into the autoclave to reach a pressure of 15 MPa. All experiments were conducted under static conditions. Table 2 lists the conditions and parameters of corrosion test. The experiment duration was 120 h. It should be noted that since the aim of this work is to study the interaction between H_2S and CO_2 during the corrosion of G20 steel, the CO_2 corrosion experiment was not conducted specifically.

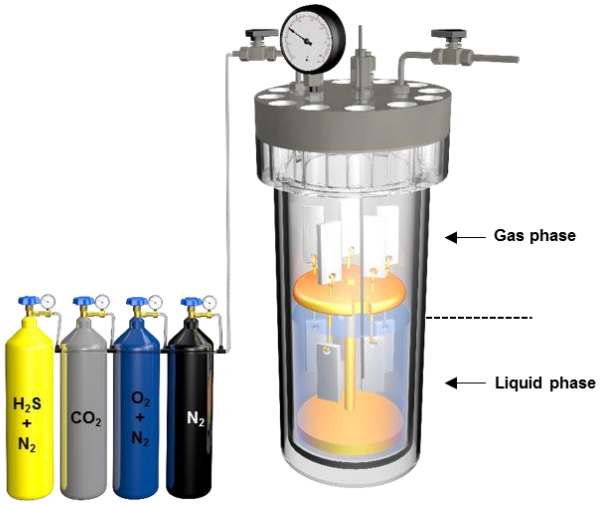

Figure 2. Schematic diagram of the setup for simulating the environment of flue gas injection in laboratory.

Table 2. Test conditions of corrosion of G20 steel in simulating flue gas injection environment.

No.	Temperature (°C)	Pressure (MPa)	CO_2 (MPa)	O_2 (MPa)	H_2S (ppmv)	Gas/Liquid Phase
1	60	15	2.25	0.21	0	Gas
2	60	15	2.25	0	600	Gas
3	60	15	2.25	0.21	600	Gas
4	60	15	2.25	0.21	0	Liquid
5	60	15	2.25	0	600	Liquid
6	60	15	2.25	0.21	600	Liquid

After the experiment, specimens for XRD and scanning electron spectroscopy (SEM, ZEISS EVO MA 15 SEM, Oberkochen, Germany) were rinsed with ethanol and dried in a vacuum oven until time came for analysis, while specimens that were used for the analysis of cross-section of corrosion products were rinsed with ethanol, dried, and immediately mounted into the epoxy resin. Specimens for weight loss measurement were brushed to mechanically remove loose corrosion products, rinsed with acetone, exposed to the Clarke solution (ASTM G103) to dissolve the remaining corrosion products [17,18], dried again in N_2 gas flow, and finally weighed.

2.3. Evaluation of Corrosion Rates

The corrosion rate was calculated as follows:

$$CR = 87,600 \frac{\Delta m}{\rho A \Delta t}, \quad (1)$$

in which CR is the corrosion rate (mm/y), Δm presents the weight loss of the specimen before and after corrosion (g), ρ is density of specimen (g/cm^3), A is area of specimen exposed to the corrosive solution (cm^2), and t is duration of corrosion (h).

2.4. Characterization of Corrosion Products

The surface morphology and the cross-sectional morphology of corrosion product formed on specimen surfaces were examined using a ZEISS EVO MA 15 SEM. The elemental composition of the corrosion products was analyzed by EDS, which was coupled with the SEM. The crystal structure of the corrosion products was investigated by X-ray diffraction on X'pert PRO with a Co-K X-ray tube (PANalytical, Almelo, The Netherlands).

3. Results

3.1. Corrosion Rates

In gas phase, it is seen that the corrosion rate in H_2S-containing environment is higher than that in O_2-containing environment (Figure 3), i.e., in the presence of 0.21 MPa O_2, the average corrosion rate in gas phase is 0.235 mm/y, while this value is as high as 0.345 mm/y in the presence of 600 ppmv H_2S. The corrosion rate increases up to 0.83 mm/y when O_2 and H_2S co-exist in the environment. This indicates that the coexistence of O_2 and H_2S makes the environment more aggressive than the presence of single component, either O_2 or H_2S. This result is in good agreement with the findings of Sun et al. in water-saturated supercritical CO_2 system [10]. They found that the accelerating effect of H_2S on the corrosion of X65 steel was greater than that of O_2, and the corrosion rates increased further with the coexistence of O_2 and H_2S.

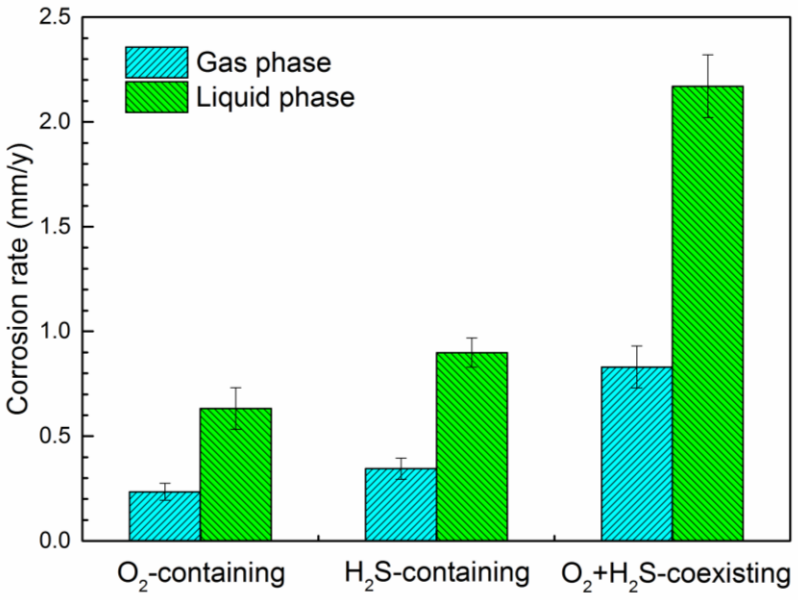

Figure 3. Corrosion rates of G20 steel in different conditions.

As a comparison, the corrosion rates of G20 steel in liquid phase under different conditions are also presented in Figure 3. Like in the gas phase, the corrosion rate of G20 steel in H_2S-containing environment is higher than that in O_2-containing environment, and the highest corrosion rate can be seen in O_2-H_2S-coexisting environment. Particularly, it is apparently that the corrosion rates in liquid phase are much higher than gas phase. For example, in the O_2-H_2S-coexisting environment, the corrosion rate of G20 steel is 2.17 mm/y in liquid phase, which is about four times higher than that in gas phase. Zhang et al. also found that the corrosion rate in liquid phase was always higher than that in gas phase in CO_2-H_2S-coexisting environment [19]. This is probably due to that the high conductivity of liquid leads to a higher electrochemical reaction rate than that in gas phase where only condensed water adsorbed on the surface of specimens.

3.2. Microstucture and Composition of Corrosion Products

3.2.1. O_2-Containing Environment

As is shown in Figure 4a,b, the distribution of corrosion products is not homogenous, and some pores can be seen from the surface image of the corrosion products. Moreover, the pores and cracks can also be seen from the cross-sectional image of the corrosion product layer (Figure 4c), suggesting that this corrosion product layer is poor in corrosion protection. The XRD results identified that the corrosion products are mainly composed of $FeCO_3$ (siderite) and FeO(OH) (goethite), as is shown in Figure 4d. The characterization peaks of ferrite are attributed to the substrate material. This result is in good agreement with the EBSD results (Figure 1), in which the ferrite is the dominant phase of G20 steel.

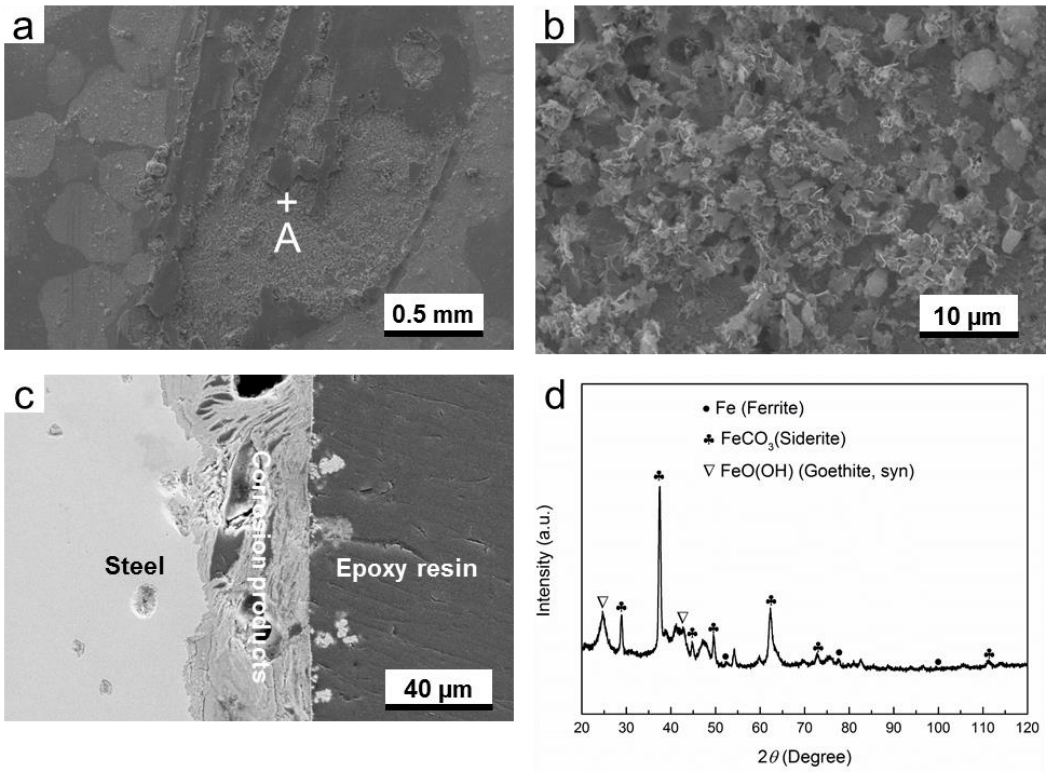

Figure 4. The characterization of corrosion products on G20 steel in gas phase in O_2-containing environment: (**a**) SEM image of the surface of corrosion products; (**b**) the higher magnification of region A marked in (**a**); (**c**) corrosion-sectional image of corrosion product layer and (**d**) XRD pattern of the corrosion products.

In the corresponding liquid phase in O_2-containing environment, it is found that the particles with different sizes are distributed on the surface of corrosion product layer (Figure 5). From the image with higher magnification as shown in Figure 5b, the prism-shaped crystals are distributed separately on the surface layer. The cross-sectional SEM image shows that lots of pores and cracks are presented in the corrosion product layer. This means that a high corrosion rate (0.632 mm/y) of G20 steel in liquid phase in O_2-containing environment must be obtained, because the corrosion product layer could not supply enough protection for the substrate. The diffraction peaks of ferrite, $FeCO_3$, Fe_3C (cementite), and FeO(OH) can be seen in the XRD pattern shown in Figure 5d. Fe_3C is the inclusions in the microstructure of the G20 steel, which has also been found in EBSD results (Figure 1).

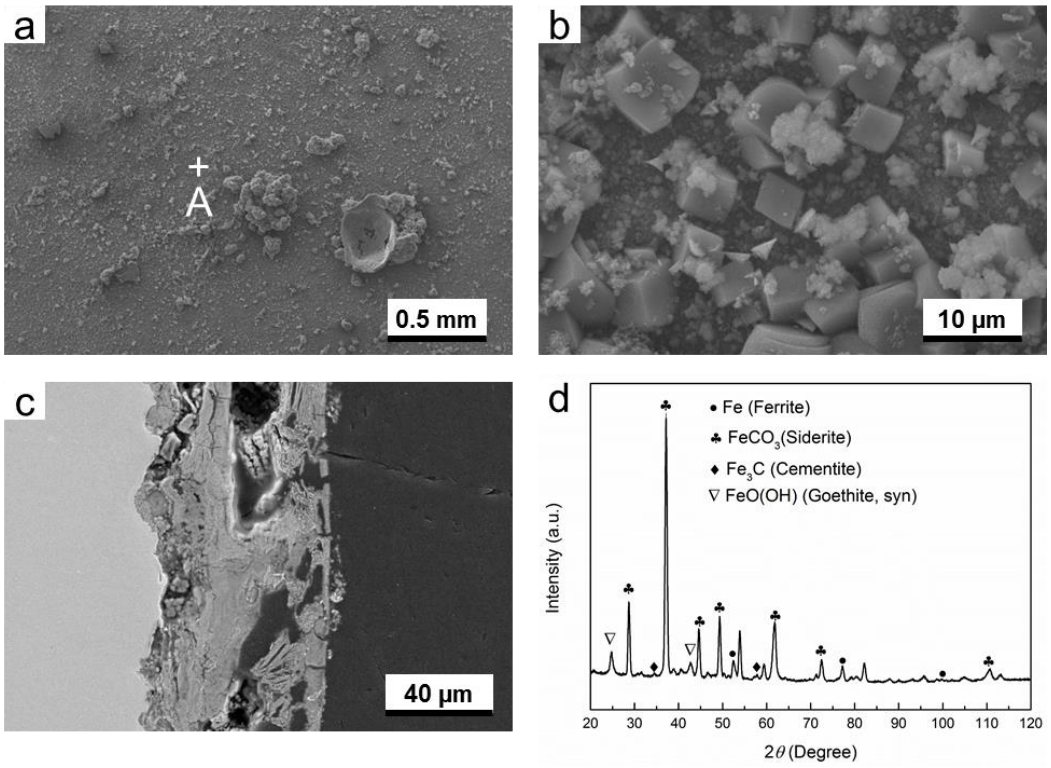

Figure 5. The characterization of corrosion products on G20 steel in liquid phase in O_2-containing environment: (**a**) SEM image of the surface of corrosion products; (**b**) the higher magnification of region A marked in (**a**); (**c**) corrosion-sectional image of corrosion products layer, and (**d**) XRD pattern of the corrosion products.

In O_2-containing environment, the thickness of corrosion product layer formed in gas phase is smaller than liquid phase. However, the corrosion product layer in gas phase is less porous than liquid phase (see Figures 4c and 5c). The difference in microstructure between both conditions probably causes the difference in corrosion rate. The XRD results indicate that composition of corrosion products for both gas and liquid phase is mainly composed of $FeCO_3$ and FeO(OH).

3.2.2. H_2S-Containing Environment

It can be seen that the microstructure of corrosion product layer is different from that formed in O_2-containing environment (Figure 6). There are a lot of needle-shaped substances distributed on the surface of corrosion products layer (Figure 6b). Numerous small cracks and pores can be seen, as shown in Figure 6c. Furthermore, the gap between the corrosion product layer and the substrate suggests poor adhesion between them. Therefore, the corrosive species can contact directly the substrate, and, subsequently, the corrosion occurs continuously. In the presence of H_2S, the composition of corrosion product layer is more complicated, which consists of $FeCO_3$, FeO(OH), and FeS (Makinawite).

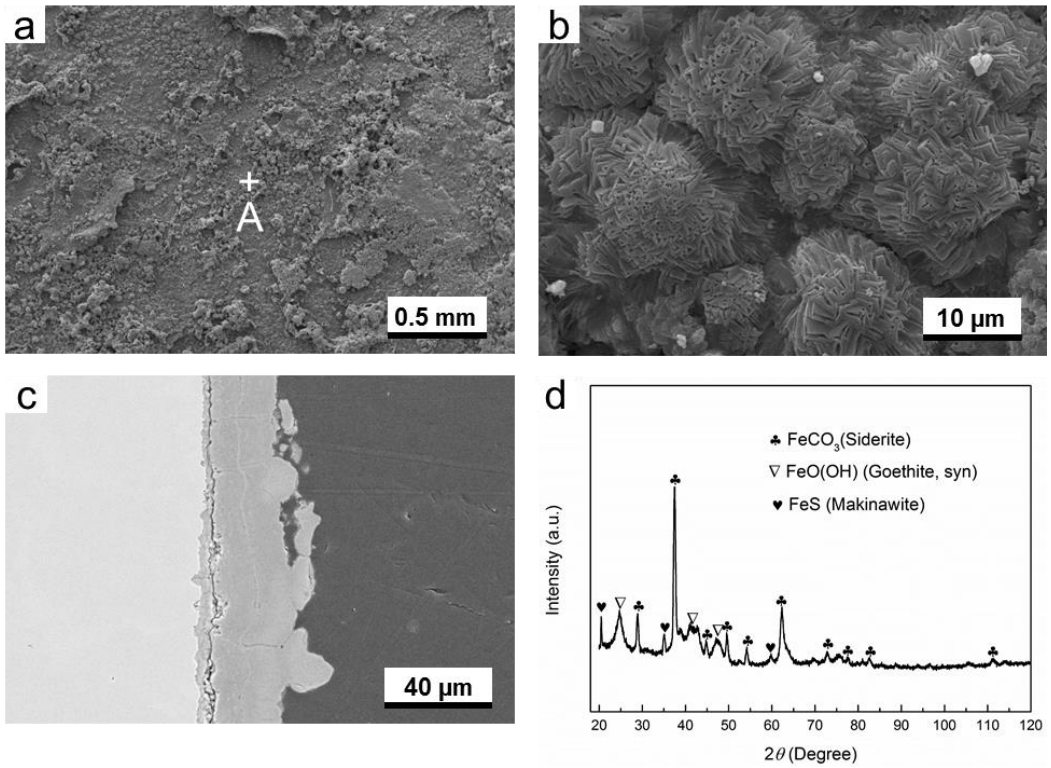

Figure 6. The characterization of corrosion products on G20 steel in gas phase in H_2S-containing environment: (**a**) SEM image of the surface of corrosion products; (**b**) the higher magnification of region A marked in (**a**); (**c**) corrosion-sectional image of corrosion product layer, and (**d**) XRD pattern of the corrosion products.

In the corresponding liquid phase, it can be seen that the structure of the corrosion products is loose, because large amount of pores and cracks are present, as shown in Figure 7b,c. The thickness of corrosion product layer is smaller than that formed in gas phase. This is probably due to the fact that the formed corrosion products are easily flaked off, and lots of corrosion products have fallen down into the solution. The presence of very strong diffraction peaks for ferrite in XRD pattern also confirms that the corrosion product layer is very thin, as is shown in Figure 7d. The composition of corrosion product formed in liquid phase is almost identical to that formed in gas phase, i.e., the corrosion products are composed of $FeCO_3$, FeO(OH), and FeS. However, the Fe_3O_4 (iron oxide) is present occasionally in this condition.

In H_2S-containing environment, it can be easily understood that the formation of $FeCO_3$ and FeS resulted from the presence of CO_2 and H_2S in the environment, respectively. According to the findings of Gao et al., the formation of Fe_3O_4 in H_2S-containing environment at high temperatures is common [20], but in this work the temperature is only 60 °C. Therefore, the occasional presence of Fe_3O_4 may be attributed to the transformation from other iron compounds, such as the oxidation of FeS [21]. FeO(OH) is possibly transferred from the oxidation of Makinawite [21], because the contact between air and corrosion product cannot be completely avoided during the period from the end of experiment in autoclave to the time of XRD measurement.

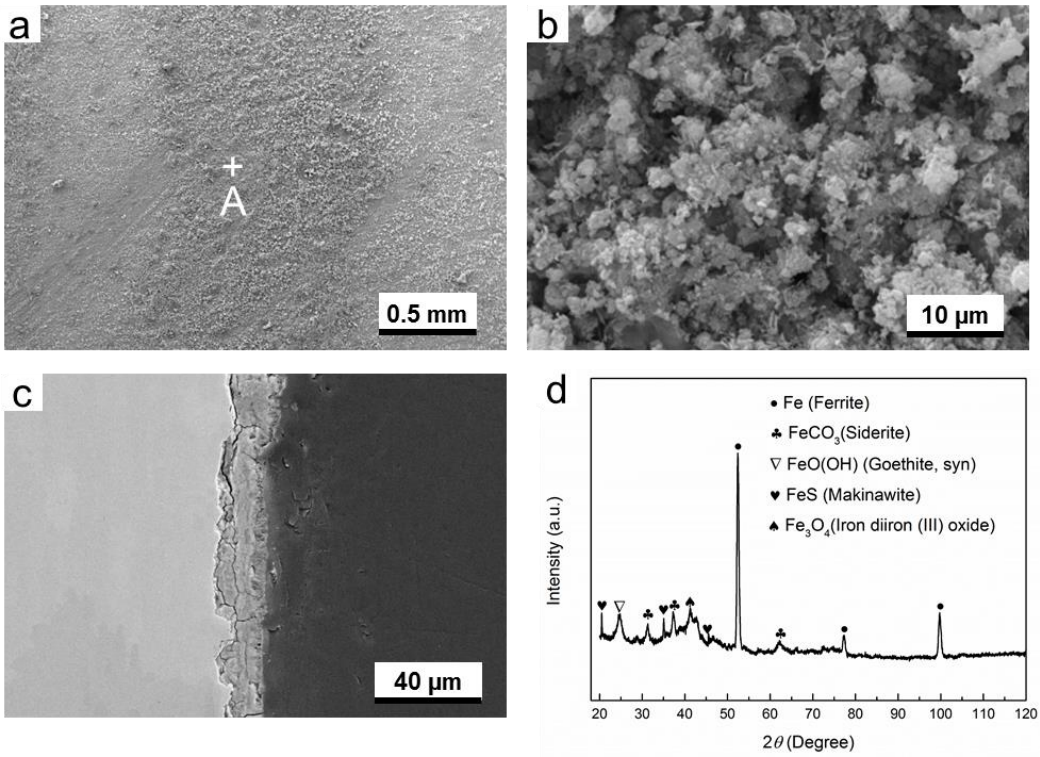

Figure 7. The characterization of corrosion products on G20 steel in liquid phase in H_2S-containing environment: (**a**) SEM image of the surface of corrosion products, (**b**) the higher magnification of region A marked in (**a**), (**c**) corrosion-sectional image of corrosion product layer, and (**d**) XRD pattern of the corrosion products.

3.2.3. O_2-H_2S-Coexisting Environment

As shown in Figure 8a–c, it is obvious that numerous cracks are present in the corrosion products layer. At the same time, a remarkable gap between the corrosion product layer and the substrate can be seen (Figure 8c), meaning a poor adhesion between them. Therefore, it can be considered that the protection ability of the corrosion product layer is extremely low when O_2 and H_2S coexist in the environment. Therefore, the highest corrosion rate (0.83 mm/y) in gas phase was obtained in this condition (Figure 3). The XRD results (Figure 8d) demonstrate that the corrosion products are composed of $FeCO_3$, FeO(OH), FeS, and S (element sulfur).

Compared with the gas phase, the corrosion product layer in liquid phase is thinner, and its distribution is not homogenous (Figure 9). This is probably because the corrosion products are very loose, and they are easily flaked off from the substrate. Otherwise, the thickness of corrosion products should be the thickest, because in this case it shows the highest corrosion rate (2.17 mm/y). After the experiment in autoclave, large amount of corrosion products was found at the bottom of the autoclave. This phenomenon also supports our speculation. The composition of corrosion products formed in liquid phase is almost the same with the gas phase. However, small amount of Fe_3O_4 is also present in this condition.

As compared with the O_2-containing environment and H_2S-containing environment, the corrosion product layer formed in O_2-H_2S-coexisting environment is more porous, suggesting a poorer protection performance. The biggest difference in composition of corrosion products among them is that the presence of element sulfur. The element sulfur may be produced from the reaction between H_2S and O_2, or the reaction between H_2S and Fe^{3+} [10], or the transformation of FeS. This will be discussed in the next section.

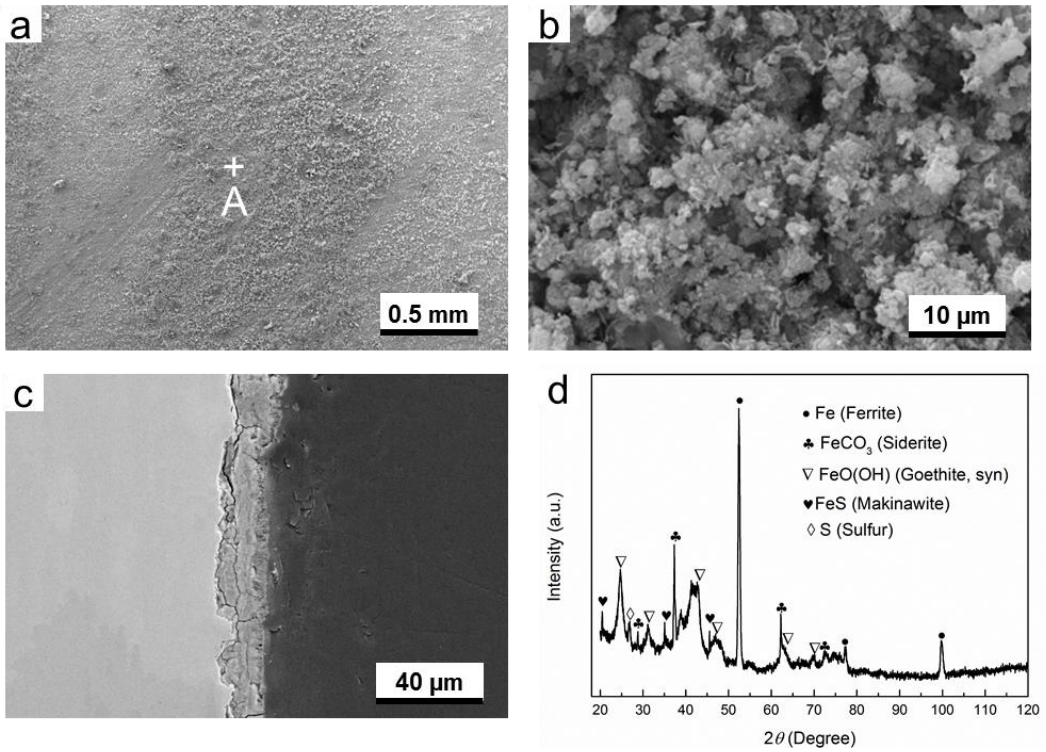

Figure 8. The characterization of corrosion products on G20 steel in gas phase in O_2-H_2S-coexisting environment: (**a**) SEM image of the surface of corrosion products, (**b**) the higher magnification of region A marked in (**a**), (**c**) corrosion-sectional image of corrosion product layer, and (**d**) XRD pattern of the corrosion products.

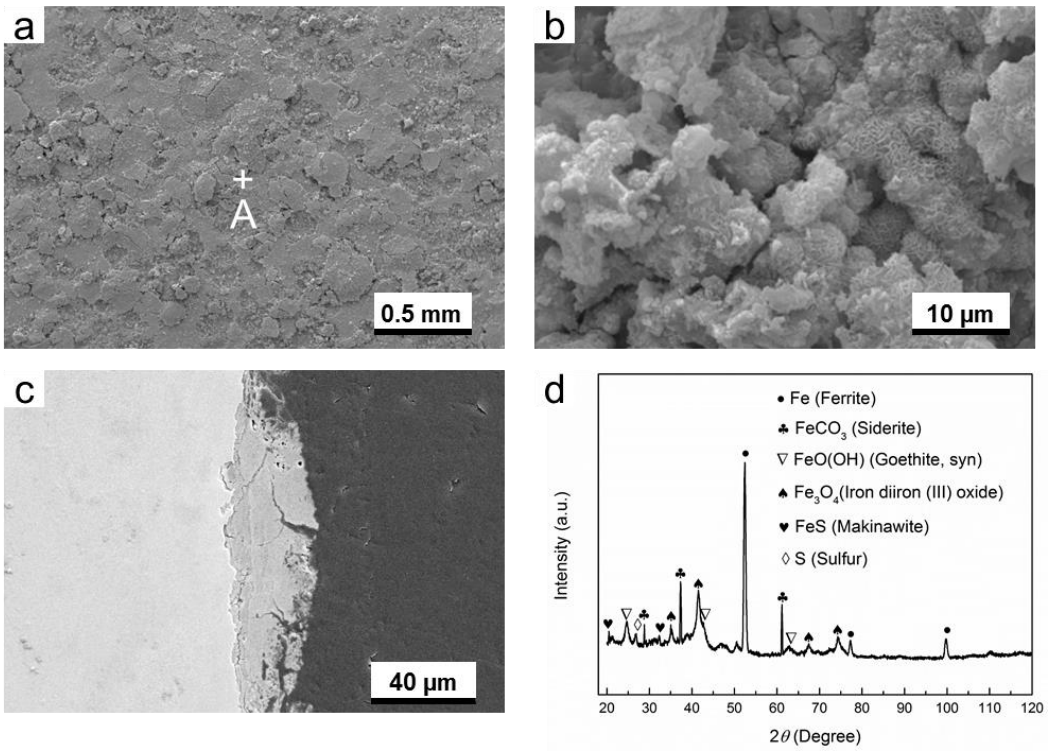

Figure 9. The characterization of corrosion products on G20 steel in liquid phase in O_2-H_2S-coexisting environment: (**a**) SEM image of the surface of corrosion products, (**b**) the higher magnification of region A marked in (**a**), (**c**) corrosion-sectional image of corrosion products layer, and (**d**) XRD pattern of the corrosion products.

4. Discussion

4.1. Corrosion Reactions and the Formation Mechanisms of Corrosion Products in Flue Gas Injection Environment

The electrochemical reactions of steel in CO_2-O_2-H_2S-coexisting environment are rather complicated, because there are various species in the solution, such as O_2, H^+, H_2CO_3, CO_3^{2-}, HCO_3^-, H_2S, HS^-, and S^{2-} [19,22–25]. These species can directly or indirectly participate in the corrosion reactions. Depending on the test conditions such as solution pH, and the partial pressure of corrosive gases, the following equations may be involved in the cathodic process:

$$O_2 + 2H_2O + 4e^- \rightarrow 4OH^-, \quad (2)$$

$$2H^+ + 2e^- \rightarrow H_2, \quad (3)$$

$$2H_2CO_3 + 2e^- \rightarrow H_2 + 2HCO_3^-, \quad (4)$$

$$2HCO_3^- + 2e^- \rightarrow H_2 + 2CO_3^{2-}, \quad (5)$$

$$2H_2S + 2e^- \rightarrow H_2 + 2HS^-, \quad (6)$$

$$2HS^- + 2e^- \rightarrow H_2 + S^{2-}. \quad (7)$$

The anodic process is primarily the dissolution of iron:

$$Fe \rightarrow Fe^{2+} + 2e^-, \quad (8)$$

In addition, the formation of corrosion product through the solid state reaction can also be considered as parts of anodic process [19]:

$$Fe + H_2CO_3 \rightarrow FeCO_3 + 2H^+ + 2e^-, \quad (9)$$

$$Fe + H_2S \rightarrow FeS_{1-x} + xHS^- + (2 - x)H^+ + 2e^-. \quad (10)$$

Figures 4–9 show that corrosion products are present on G20 steel surface in each condition. Generally, the formation of corrosion products follows the solid state reaction mechanism and/or precipitation mechanism. The corrosion products formed in different conditions in this work include $FeCO_3$, FeO(OH), FeS, Fe_3O_4, and S.

$FeCO_3$ is a common CO_2 corrosion product. Once Fe^{2+} and CO_3^{2-} are present at the steel/solution interface at sufficiently high concentrations, which make the product of $[Fe^{2+}] \times [CO_3^{2-}]$ exceed the solubility product of $FeCO_3$, precipitation and crystal growth will occur [26], as described in Equation (11):

$$Fe^{2+} + CO_3^{2-} \rightarrow FeCO_3. \quad (11)$$

In this study, $FeCO_3$ can be detected in the corrosion product layer formed in all the conditions. This is attributed to the relatively high CO_2 partial pressure and high pH in the experimental environment. The CO_2 partial pressure in each condition was up to 2.25 MPa, and the pH in corrosive solution was 7.0, which favored the formation of $FeCO_3$ [26].

The formation of FeO(OH) resulted from the reactions related to O_2. Yamashita et al. employed in situ XRD to detect the composition of corrosion products on iron in the O_2-containing environment and found the initial corrosion products should be the mixture of $Fe(OH)_2$ and $Fe(OH)_3$, which are formed as the following equations [27]:

$$Fe^{2+} + 2OH^- \rightarrow Fe(OH)_2, \quad (12)$$

$$4Fe(OH)_2 + O_2 + 2H_2O \rightarrow 4Fe(OH)_3. \quad (13)$$

These initial corrosion products are subsequently transformed to β-FeO(OH), α-FeO(OH), γ-FeO(OH), and/or Fe_3O_4, depending on the environment. In this study, α-FeO(OH) (goethite) was only detected (Figures 4–9). It should be pointed out that small amount of FeO(OH) in the corrosion products formed in H_2S-containing environment was also detected (Figures 6 and 7). This is possibly due to the transfer from FeS (Makinawite) to FeO(OH) when the FeS is exposed to the O_2-containing environment [21,28,29]. During the period from the end of experiment in autoclave to the time of XRD measurement, the contact between air and corrosion product cannot be completely avoided. Therefore, this speculation could be true.

Mackinawite (FeS) is widely considered to be the initial corrosion product in H_2S corrosion due to its rapid formation kinetics [30,31]. It is generally considered that it can convert into other types of iron sulfide due to its meta-stability [31]; however, in this work only Mackinawite was detected in the corrosion product formed in H_2S-containing environment and O_2-H_2S-coexisting environment, as is shown in Figures 6–9. The formation of FeS can be expressed as the following equation:

$$Fe^{2+} + HS^- \rightarrow FeS + H^+. \quad (14)$$

Like the formation of $FeCO_3$, as long as Fe^{2+} and HS^- are present at the steel/solution interface at sufficiently high concentrations that make the value of $[Fe^{2+}] \times [HS^-]/[H^+]$ exceed the solubility product of FeS, precipitation and crystal growth will occur. As mentioned above, FeS can be readily oxidized to form FeO(OH) when it is exposed to an O_2-containing environment, as expressed in Equation (15) [30]:

$$4FeS + 3O_2 + 2H_2O \rightarrow 4FeO(OH) + 4S. \quad (15)$$

Therefore, the FeO(OH) in H_2S-containing environment can be detected. Upon further exposure to O_2-containing environment, the FeO(OH) can transform to Fe_3O_4 [30]. Smith et al. even proposed that FeS may be rapidly oxidized to Fe_3O_4 and sulfur by [32]:

$$FeS + 3O_2 \rightarrow Fe_3O_4 + S. \quad (16)$$

That is why a small amount of Fe_3O_4 could be detected in H_2S-containing environment (Figures 7 and 9).

In O_2-H_2S-coexisting environment, the formation of elemental sulfur probably resulted from the reactions between H_2S and O_2 and Fe^{3+} [10,33–35]:

$$2H_2S + O_2 \rightarrow 2S + 2H_2O, \quad (17)$$

$$H_2S + 2Fe^{3+} \rightarrow S + 2H^+ + 2Fe^{2+}. \quad (18)$$

At the same time, the transformation of FeS in O_2-containing environment can also generate the elemental sulfur, as expressed in Equations (15) and (16).

4.2. The Coupling Effect of O_2 and H_2S on the Flue Gas Injection Corrosion

Compared with the O_2-containing environment and H_2S-containing environment, the weight loss results indicate that the coexistence of O_2 and H_2S causes a more obvious accelerating effect on corrosion rate of G20 in both gas phase and liquid phase. Taking the gas phase as an example, the corrosion rates are 0.235 mm/y and 0.345 mm/y in O_2-containing environment and H_2S-containing environment, respectively. However, the corrosion rate in O_2-H_2S-coexisting environment sharply increases up to 0.830 mm/y, which is much higher than the sum of corrosion rates in O_2-containing environment and H_2S-containing environment (Figure 3). This means that there is an interaction effect between O_2 and H_2S during the corrosion process, resulting in the more serious corrosion. Sun et al. thought that there was a synergistic effect between O_2 and H_2S on corrosion of steel in supercritical

CO_2 system [10]. In flue gas injection environment, a similar tendency of corrosion rate has been found in this work.

On the one hand, as expressed in Equations (2) and (6), O_2 and H_2S can directly participate in the cathodic reaction of steel, thereby increasing the corrosion rate. For H_2S, following its dissolution in the solution, the pH will decrease and the corrosion rate will increase further. On the other hand, the reaction between O_2 and H_2S can generate elemental sulfur, which significantly accelerates the corrosion of carbon steel [10,34–36]. The corrosion mechanism of steel triggered by elemental sulfur has not yet reached consensus understanding. Different researchers have proposed different mechanisms, such as the direct reaction of elemental sulfur with iron [35], the electrochemical reaction of polysulfide with iron [36], and the corrosion caused by the formation of acid due to the hydrolysis of sulfur [37]. Regardless of the corrosion mechanism, elemental sulfur generated from the reaction of O_2 and H_2S can further accelerate the corrosion rate of steel. Therefore, a coupling effect on corrosion of G20 steel in flue gas injection environment has been found. The exact accelerating mechanism of elemental sulfur on corrosion still needs further investigation.

5. Conclusions

In simulating the flue gas injection environment, the coupling effect of O_2 and H_2S on corrosion of G20 steel has been found. In the gas phase environment, the corrosion rates in O_2-containing environment and H_2S-containing environment are 0.235 mm/y and 0.345 mm/y, respectively. However, the corrosion rate in the O_2-H_2S-coexisting environment is as high as 0.83 mm/y, which is much higher than the sum of corrosion rates of both the O_2-containing environment and the H_2S-containing environment. Similarly, the corrosion rate in liquid phase in the O_2-H_2S-coexisting environment is also higher than the sum of corrosion rate in both environments. It can be considered that this coupling effect resulted from the presence of elemental sulfur, which was mainly produced from the reaction between O_2 and H_2S.

The corrosion product of G20 formed in simulating flue gas injection environment consists of $FeCO_3$, FeO(OH), FeS, Fe_3O_4, and S. It is also found that the corrosion product layer is porous and non-protective. Furthermore, the generation of elemental sulfur increases the corrosion of steel.

Author Contributions: Data curation, X.Z. and Y.W.; Formal analysis, X.Z., L.C. and X.S.; Funding acquisition, J.L., L.C. and X.S.; Investigation, X.Z. and Y.W.; Project administration, X.Z., J.L., L.C. and X.S.; Supervision, J.L., L.C. and X.S.; Writing—original draft, X.Z.; Writing—review & editing, J.L. and X.S.

Funding: This research was funded by [National Science Foundation of China] grant number [51474183].

Conflicts of Interest: The authors declare no conflict of interest.

References

1. Dong, M.; Huang, S. Flue gas injection for heavy oil recovery. *J. Can. Petrol. Technol.* **2002**, *41*, 44–50. [CrossRef]
2. Yee, C.T.; Stroich, A. Flue gas injection into a mature SAGD steam chamber at Dover project (formerly UTF). In Proceedings of the Canadian International Petroleum Conference, Calgary, AB, Canada, 11–13 June 2002.
3. Kahyarian, A.; Singer, M.; Nesic, S. Modeling of uniform CO_2 corrosion of mild steel in gas transportation systems: A review. *J. Nat. Gas Sci. Eng.* **2016**, *29*, 530–549. [CrossRef]
4. De Warrd, C.; Lotz, U.; Milliams, D.E. Predictive model for CO_2 corrosion engineering in wet natural gas pipelines. *Corrosion* **1991**, *47*, 976–985. [CrossRef]
5. Nesic, S.; Lunde, L. Carbon dioxide corrosion of carbon steel in two-phase flow. *Corrosion* **1994**, *50*, 717–727. [CrossRef]
6. Gao, M.; Pang, X.; Gao, K. The growth mechanism of CO_2 corrosion product films. *Corros. Sci.* **2011**, *53*, 557–568. [CrossRef]
7. Li, W.; Pots, B.F.M.; Zhong, X.; Nesic, S. Inhibition of CO_2 corrosion of mild steel-steel of mechanical effects of highly turbulent disturbed flow. *Corros. Sci.* **2017**, *126*, 208–226. [CrossRef]

8. Heuer, J.K.; Stubbins, J.F. An XPS characterization of $FeCO_3$ films from CO_2 Corrosion. *Corros. Sci.* **1999**, *41*, 1231–1243. [CrossRef]
9. Choi, Y.S.; Nesic, S.; Young, D. Effect of impurities on the corrosion behavior of CO_2 transmission pipeline steel in supercritical CO_2-water environments. *Environ. Sci. Technol.* **2010**, *44*, 9233–9238. [CrossRef] [PubMed]
10. Sun, J.; Sun, C.; Zhang, G.; Li, X.; Zhao, W.; Jiang, T.; Liu, H.; Cheng, X.; Wang, Y. Effect of O_2 and H_2S impurities on the corrosion behavior of X65 steel in water-saturated supercritical CO_2 system. *Corros. Sci.* **2016**, *107*, 31–40. [CrossRef]
11. Lin, X.; Liu, W.; Wu, F.; Xu, C.; Dou, J.; Lu, M. Effect of O_2 on corrosion of 3Cr in high temperature and high pressure CO_2-O_2 environment. *Appl. Surf. Sci.* **2015**, *329*, 104–115. [CrossRef]
12. Abelev, E.; Sellberg, J.; Ramanarayanan, T.A.; Bernasek, S.L. Effect of H_2S on Fe corrosion in CO_2-saturated brine. *J. Mater. Sci.* **2009**, *44*, 6767–6781. [CrossRef]
13. Choi, Y.S.; Nesic, S.; Ling, S. Effect of H_2S on the CO_2 corrosion of carbon steel in acidic solutions. *Electrochim. Aata* **2011**, *56*, 1752–1760. [CrossRef]
14. Sun, C.; Sun, J.; Wang, Y.; Lin, X.; Li, X.; Cheng, X.; Liu, H. Synergistic effect of O_2, H_2S and SO_2 impurities on the corrosion behavior of X65 steel in water-saturated supercritical CO_2 system. *Corros. Sci.* **2016**, *107*, 193–203. [CrossRef]
15. Brown, J.; Graver, B.; Gulbrandsen, E.; Dugstad, A.; Morland, B. Update of DNV recommended practice RP-J202 with focus on CO_2 corrosion with impurities. *Energy Procedia* **2014**, *63*, 2432–2441. [CrossRef]
16. Xiang, Y.; Choi, Y.-S.; Yang, Y.; Nesic, S. Corrosion of carbon steel in MDEA-based CO_2 capture plants under regenerator conditons: Effect of O_2 and H_2S heat-stable salts. *Corrosion* **2015**, *71*, 30–37. [CrossRef]
17. Clarke, S.G. The use of inhibitors (with special reference to antimony) in the selective removal of metallic coatings and rust. *Trans. Electrochem. Soc.* **1936**, *69*, 131–144. [CrossRef]
18. Jin, P.; Bota, G.; Robbins, W.; Nesic, S. Analysis of oxide scales formed in the naphthenic acid corrosion of carbon steel. *Energy Fuel* **2016**, *30*, 6853–6862. [CrossRef]
19. Zhang, G.A.; Zeng, Y.; Guo, X.P.; Jiang, F.; Shi, D.Y.; Chen, Z.Y. Electrochemical corrosion behavior of carbon steel under dynamic high pressure H_2S/CO_2 environment. *Corros. Sci.* **2012**, *65*, 37–47. [CrossRef]
20. Gao, S.; Brown, B.; Young, D.; Singer, M. Formation of iron oxide and iron sulfide at high temperature and their effects on corrosion. *Corros. Sci.* **2018**, *135*, 167–176. [CrossRef]
21. Fujinami, M.; Ujihira, Y. Chemical state analysis of corrosion products on a steel in H_2S-N_2 and H_2S-O_2-N_2 environment by means of conversion electron mössbauer spectroscopy. *Appl. Surf. Sci.* **1984**, *17*, 276–284. [CrossRef]
22. De Waard, C.; Milliams, D.E. Carbonic acid corrosion of steel. *Corrosion* **1975**, *31*, 177–181. [CrossRef]
23. Nesic, S.; Postlethwaite, J.; Olsen, S. An electrochemical model for prediction of corrosion of mild steel in aqueous carbon dioxide solutions. *Corrosion* **1996**, *52*, 280–294. [CrossRef]
24. Zheng, Y.; Brown, B.; Nesic, S. Electrochemical study and modeling of H_2S corrosion of mild steel. *Corrosion* **2014**, *70*, 351–365. [CrossRef]
25. Zheng, Y.; Ning, J.; Brown, B.; Nesic, S. Electrochemical model of mild steel corrosion in a mixed H_2S/CO_2 aqueous environment in the absence of protective corrosion product layers. *Corrosion* **2015**, *71*, 316–325. [CrossRef]
26. Li, W.; Brown, B.; Young, D.; Nesic, S. Investigation of pseudo-passivation of mild steel in CO_2 corrosion. *Corrosion* **2014**, *70*, 294–302. [CrossRef]
27. Yamashita, M.; Konishi, H.; Kozakura, T.; Mizuki, J.; Uchida, H. In situ observation of initial rust formation process on carbon steel under Na_2SO_4 and NaCl solution films with wet/dry cycles using synchrotron radiation X-rays. *Corros. Sci.* **2005**, *47*, 2492–2498. [CrossRef]
28. Ning, J.; Zheng, Y.; Young, D.; Brown, B.; Nesic, S. Thermodynamic study of hydrogen sulfide corrosion of mild steel. *Corrosion* **2014**, *70*, 375–389. [CrossRef]
29. Ning, J.; Zheng, Y.; Young, D.; Brown, B.; Nesic, S. A Thermodynamic Model for the Prediction of Mild Steel Corrosion Products in an Aqueous Hydrogen Sulfide Environment. *Corrosion* **2015**, *71*, 945–960. [CrossRef]
30. Craig, B.D. The nature of iron sulfides formed on steel in an H_2S-O_2 environment. *Corrosion* **1979**, *35*, 136–138. [CrossRef]
31. Bourdoiseau, J.A.; Jeannin, M.; Sabot, R.; Rémazeiles, C.; Refait, P. Characterisation of macknawite by Raman spectroscopy: Effects of crystallization, drying and oxidation. *Corros. Sci.* **2008**, *50*, 3247–3255. [CrossRef]

32. Smith, S.N.; Pacheco, J.L. Prediction of corrosion in slightly sour environments. In Proceedings of the NACE International's Annual Conference and Exposition, Denver, CO, USA, 7–11 April 2002.
33. Steudel, R. Mechanism for the formation of elemental sulfur from aqueous sulfide in chemical and microbiological desulfurization processed. *Ind. Eng. Chem. Res.* **1996**, *35*, 1417–1423. [CrossRef]
34. Dugstad, A.; Halseid, M.; Morland, B. Experimental techniques used for corrosion testing in dense phase CO_2 with flue gas impurities. In Proceedings of the NACE International's Annual Conference and Exposition, San Antonio, TX, USA, 9–13 March 2014.
35. Fang, H.; Young, D.; Nesic, S. Corrosion of Mild Steel in the Presence of Elemental Sulfur. In Proceedings of the NACE International's Annual Conference and Exposition, New Orleans, LA, USA, 16–20 March 2008.
36. Macdonald, D.D.; Roberts, B.; Hyne, J.B. The corrosion of carbon steel by wet elemental sulfur. *Corros. Sci.* **1978**, *18*, 411–425. [CrossRef]
37. Boden, P.J.; Maldonado-Zagal, S.B. Hydrolysis of elemental sulfur in water and its effects on the corrosion of mild steel. *Br. Corros. J.* **1982**, *17*, 116–120. [CrossRef]